

11th CIRP Conference on Photonic Technologies [LANE 2020] on September 7-10, 2020

Influence of process gas during powder bed fusion with laser beam of Zr-based bulk metallic glasses

Jan Wegner^{a*}, Maximilian Frey^b, Stefan Kleszczynski^a, Ralf Busch^b, Gerd Witt^a

^a Chair of Manufacturing Technology, University Duisburg-Essen, Lotharstraße 1, 47057 Duisburg, Germany

^b Chair of Metallic Materials, Saarland University, Campus C6.3, 66123 Saarbrücken, Germany

* Corresponding author. Tel.: +492033793075; fax: +492033791530. E-mail address: jan.wegner@uni-due.de

Abstract

Zr-based bulk metallic glasses offer a unique combination of hardness, high strength, and high elastic limits. Yet, manufacturable size and complexity are limited due to the required cooling rates. Short laser-material interaction times together with layer-wise and selective energy input allows the laser powder bed fusion process to largely overcome those restrictions. Still, the complex process-material interactions inhere numerous uncertainties. In the present work, additively manufactured Zr-based bulk metallic glasses produced under three different process gases are investigated by calorimetry, x-ray diffraction, and bending tests. A strong dependence between the thermophysical properties, flexural strength, and the applied atmosphere is found.

© 2020 The Authors. Published by Elsevier B.V.

This is an open access article under the CC BY-NC-ND license (<http://creativecommons.org/licenses/by-nc-nd/4.0/>)

Peer-review under responsibility of the Bayerisches Laserzentrum GmbH

Keywords: Laser powder bed fusion; bulk metallic glasses; process gas; mechanical properties; crystallization

1. Introduction

Additive manufacturing is steadily emerging as a production method in the recent decade. Among the different techniques, the powder bed fusion of metals using a laser beam (PBF-LB/M) established as the most promising process for the efficient fabrication of highly complex and customized shapes. The design freedom is especially desirable in the medical, automotive, and aerospace industries, driving PBF-LB/M-manufactured components to series production [1, 2]. Such applications often demand advanced material performance. Apart from new geometrical possibilities, the layer-wise build-up process combined with highly dynamic laser exposure favors the creation of non-equilibrium microstructures, hence creating further potential for functional parts and material design [3, 4]. In this context, the PBF-LB/M process inaugurates new opportunities in the fabrication of bulk metallic glasses (BMGs). High cooling rates between

10^4 - 10^6 K/s combined with the layer-wise energy input allows for largely suppressed crystallization and thus surpasses the current possibilities given by casting methods [5–7]. The amorphous microstructure of Zr-based BMGs leads to high strength, elastic limits of 2 % or more, and high corrosion resistance [8]. Furthermore, the isotropic and homogenous mechanical properties of BMGs are especially desirable for additively manufactured parts [9]. However, the PBF-LB/M process is featured by complex multi-physical laser-material interactions. Respectively, the processing of BMGs inhere additional challenges, since not only lack of fusion but also crystallization must be prevented through a careful parameter selection to retain the aspired mechanical properties of BMGs [6, 10, 11]. The crystallization of Zr-based BMGs during PBF-LB/M is strongly related to increased energy inputs applied by the process parameters. The detrimental phase formations not only consist of primary crystalline phases such as Zr_2Cu but also oxide phases [11, 12]. Oxygen impurities, therefore, play a

crucial role for the glass-forming ability (GFA) of Zr-based BMGs regarding PBF-LB/M. Bordeenithikasem et al. for instance report in [13] that crystallization, and hence the resulting mechanical properties, are strongly affected by the oxygen content within the fabricated material. Further, Pacheco et al. investigated the thermal stability of PBF-LB/M manufactured AMZ4 and observed the formation of nanocrystalline oxides [12]. Respectively deteriorated mechanical properties in dependence on the oxygen contamination were also reported in [14]. This further leads to questions about the impact of the applied shielding gases during PBF-LB/M. In this context, not only the influence of residual oxygen contamination within the process atmosphere but also the gas-material interactions may play a crucial role regarding the resulting mechanical properties and the economic aspects, since laboratory-grade gases can be a non-negligible cost driver. Studies addressing the atmosphere during laser powder bed fusion are rare [15, 16]. The established shielding gases in PBF-LB/M are N₂ and Ar [17]. While argon as a noble gas is inert, N₂ can dissolve, react, and form nitrides [18]. Liu et al. report in [19] that the GFA of Zr-based BMGs is promoted by nitrogen-doping between 1000 and 3000 appm during casting in a Cu₄₉Zr₄₄Al₇ alloy by suppressing the formation of the primary Zr-Cu-phase, inhering potential benefit for the application in PBF-LB/M-process. Conventional welding techniques on the other hand often apply gas mixtures subjecting the particular requirements, for instance by H₂ addition. Due to its high thermal conductivity and oxygen-reducing chemical activity, the influence of H₂ doped gases in the PBF-LB/M of BMGs appears promising in order to reduce nano-crystalline oxide formation during the process and potentially be beneficial to increase local cooling rates [20]. Regarding the material properties, microalloying of H₂ is reported to enhance GFA and plasticity in casted Zr-based BMGs. Dong et al. report that additions of 10 - 30 % H₂ led to increased free volumes and enhanced plastic strain [21]. This study aims to evaluate the possibilities for process optimization of PBF-LB/M fabrication of Zr-based BMGs regarding the used process gas. Therefore, PBF-LB/M-manufactured samples are systematically analyzed in terms of their microstructure, thermophysical properties, and mechanical performance. Specimens produced under high-purity argon are compared to samples produced under less expensive, commercial purity N₂ process gas as well as a commercial purity argon-hydrogen mixture.

2. Experimental procedure

2.1. PBF-LB/M process

Argon atomized powder with a nominal chemical composition of Zr_{59.3}Cu_{28.8}Al_{10.4}Nb_{1.5} (in at. %) and an average particle size x_{50} of 23.65 μm was provided by Heraeus GmbH. The material was processed on an M100 PBF-LB/M system (eos GmbH) equipped with a 1064 nm wavelength fiber laser and a nominal spot-size d of 40 μm. Three different shielding gases were investigated: N₂ “N40” with 99.99 vol.% purity, “ARCAL prime” 99.998 vol.% Ar by Air Liquide GmbH, and the argon-hydrogen mixture “Varigon® H2” containing

2 vol.% hydrogen (Ar₉₈H₂) provided by Linde with a purity of 99.95 vol.% were investigated in three PBF-LB/M processes. The residual oxygen level was held below 0.05 ± 0.02 vol.%, as measured by the integrated oxygen sensor of the PBF-LB/M machine. Cubes with an edge length of 5 mm were processed to determine the influence of the respective gas on the processable parameter windows. Based on King et al. [22] a quantification of the energy deposition during PBF-LB/M dependent on the process parameters laser power P and scan speed v for the conduction and keyhole mode during melting can be given by (1):

$$\frac{\Delta H}{h_s} = \frac{A \cdot P}{h_s \cdot \pi \cdot \sqrt{\alpha \cdot v} \cdot d^3} \quad (1)$$

The absorptivity A , the melting enthalpy h_s , and the thermal diffusivity α are considered as given intrinsic material properties throughout the experimental procedure of this study. Therefore, the energy deposition is proportional to the ratio of the applied laser power and the root of the scan speed [22,23] (2):

$$\Delta H \sim \frac{P}{\sqrt{v}} \quad (2)$$

In contrast to other approaches, such as line energy density (P/v), here the laser power is considered to have a stronger impact on the energy deposition than the scan speed. This is in accordance with Tsai et al., who showed that the peak temperatures originating from exposure with a gaussian laser beam are proportional to the ratio of P/\sqrt{v} [23, 24]. Therefore, the applied process parameters are further represented by e_i as the ratio of P/\sqrt{v} . In this context, e_i was varied between 894 and 1375 $mW/\sqrt{ms^{-1}}$. Volumetric process parameters were kept constant at a layer thickness $d_s = 20$ μm and hatch distance $h = 40$ μm. For the mechanical characterization, four bending beams were fabricated in horizontal alignment to the bending direction. The beams were built with a length of 25.2 mm, a height 2.8 mm, and a width of 1.9 mm, with respect to the built orientation and evaluated by three-point bending. The process parameters were set based on Wegner et al. in [14], applying an e_i of 894 $mW/\sqrt{m \cdot s^{-1}}$.

2.2. Structural and mechanical analysis

After processing, the cubic samples were cut in half along the building direction and prepared for further analysis. To conduct microscopy and hardness indentation, one half of each cube was embedded in epoxy and further ground and polished down to 1 μm diamond suspension. The intrinsic porosity was then determined through optical density measurements using a BX50M light microscope together with the stream essential software by Olympus GmbH. Hardness indentation was performed according to DIN EN ISO 6507-1 (HV5) on polished cross-sections and was averaged over five measurements per sample. Bending beams were sanded and tested via three-point flexural bending with a Shimadzu testing machine as explained in detail in [14].

2.3. Thermophysical analysis

In order to analyze the influence of the shielding gas on the thermophysical properties, the remaining half of each cube was analyzed by means of x-ray diffraction (XRD) and differential scanning calorimetry (DSC). An X'Pert Pro MPD (Panalytical) diffractometer was used, equipped with a copper tube emitting K_{α} radiation with a wavelength of 1.5406 Å. The angular angle 2θ (Bragg angle) was scanned from 20° to 50° . DSC scans were performed with a Perkin Elmer Diamond DSC applying a heating rate of 60 K/min from 323 K to 753 K. The samples were measured in aluminum crucibles under argon flow.

3. Results and discussion

3.1. Influence on the structural properties

The application of the Ar and Ar_{98}H_2 atmosphere enabled stable processing of the entire range of investigated parameter range. On the contrary, the N_2 atmosphere led to a narrowed processable range. Here, samples processed with an e_i -value above $1230 \text{ mW}/\sqrt{\text{m}} \cdot \text{s}^{-1}$, had to be excluded from exposure during the process, due to the collision of the samples with the recoater blade. The reduced process stability of samples processed under N_2 was the result of distinctive stress-induced cracking along the contour surfaces and occasionally in the boundary surface towards the substrate, as exemplarily shown in (Fig. 1).

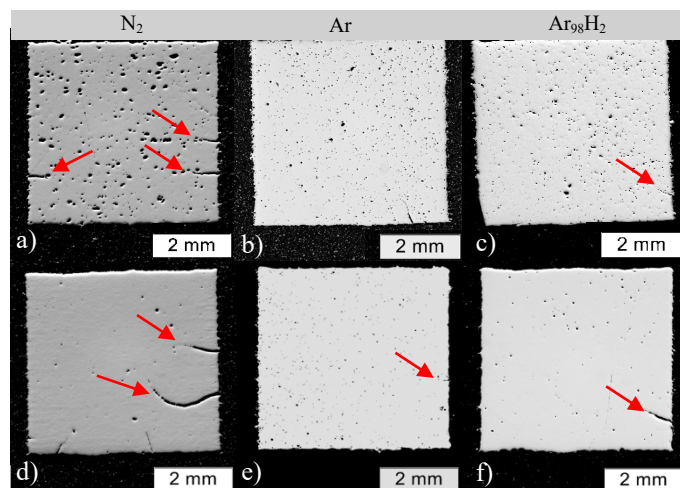


Fig. 1. Exemplarily cross sections of samples processed under N_2 , Ar and Ar_{98}H_2 comparing e_i (a)-(c): 894 and (d)-(f): 1125 $\text{mW}/\sqrt{\text{m}} \cdot \text{s}^{-1}$. Cracks are marked with red arrows.

As illustrated in Fig. 2, the relative density of the investigated parameter window resulted in relative densities above $\sim 99\%$ throughout the sample series. With increasing energy input, a further decreasing porosity was observed. Voids occur as mostly spherical gas pores and lack of fusion for energy levels below $1000 \text{ mW}/\sqrt{\text{m}} \cdot \text{s}^{-1}$, while with increasing energy input only spherical gas pores remain (compare Fig. 1). Among the compared gases, Ar led to a slightly increased relative density compared to N_2 and Ar_{98}H_2 . At ambient conditions (300 K and 100 kPa), Ar inheres with

$17.9 \text{ mW}/\text{mK}$ the lowest thermal conductivity compared to N_2 ($26 \text{ mW}/\text{mK}$) and Ar_{98}H_2 ($\sim 21.18 \text{ mW}/\text{mK}$), which contributes to increased temperatures within the melt pool and the heat-affected zone [25], hence decreased lack of fusion is expected [26]. However, the influence is subordinated compared to the energy input, since the heat convection through the gas has a minor influence on the melt pool temperature of the PBF-LB/M process and the relative density [15, 27].

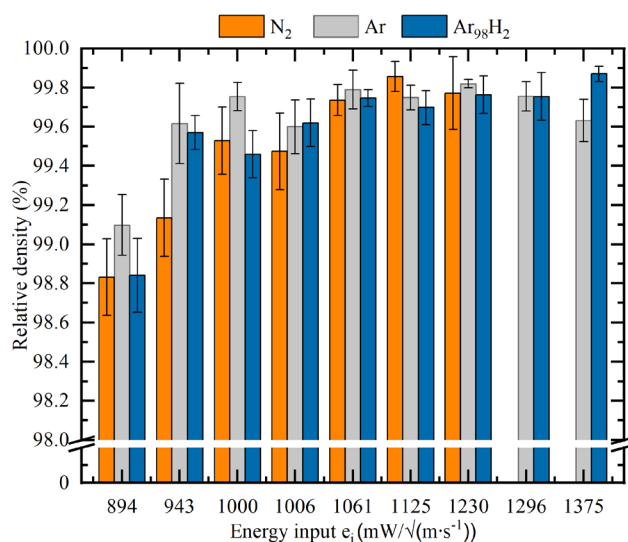


Fig. 2. Optically measured relative density in dependence of the energy input e_i for N_2 , Ar, and Ar_{98}H_2 -shielding gas. N_2 samples processed with an $e_i > 1230 \text{ mW}/\sqrt{\text{m}} \cdot \text{s}^{-1}$ had to be excluded from further exposure

3.2. Influence on the thermophysical properties

Exemplary DSC-scans of three samples produced under N_2 , Ar, and Ar_{98}H_2 with identical parameter sets, thus equivalent energy inputs of $894 \text{ mW}/\sqrt{\text{m}} \cdot \text{s}^{-1}$ are shown in Fig. 3a). At first glance, all curves show, in principle, the typical behavior of amorphous AMZ4 [14, 28]. A glass transition occurs at about 673 K as a rise of the heat flow from the glassy state level to the supercooled liquid (SCL) state level. At about 730 K, the SCL starts to crystallize as indicated by a massive exothermal event in the heat flow curve. The enthalpy of crystallization ΔH_x is defined by the integration over the respective exothermal event that starts at the end of the supercooled liquid state, as illustrated by the dotted lines in Fig. 3a). Fig. 3b) compares the obtained ΔH_x values for the fabricated samples. The usage of Ar and Ar_{98}H_2 resulted in ΔH_x values in the order of 4300–4600 J/mol, which is a typical value for amorphous PBF-LB/M-processed AMZ4 samples [14]. Here, ΔH_x only decreases for e_i values above $1230 \text{ mW}/\sqrt{\text{m}} \cdot \text{s}^{-1}$ using Ar_{98}H_2 and $1375 \text{ mW}/\sqrt{\text{m}} \cdot \text{s}^{-1}$ in Ar. Thus, a relative density of $\sim 99,8\%$ can be achieved without distinct crystallization within the samples. Different behavior is found for samples produced under N_2 . Here, ΔH_x only reaches about 4100 J/mol for low energy inputs and further decreases for growing e_i values, indicating partially crystalline samples after the PBF-LB/M process. Therefore, within the investigated framework of this study, the usage of “N40” N_2 does not allow the fully amorphous processing of AMZ4.

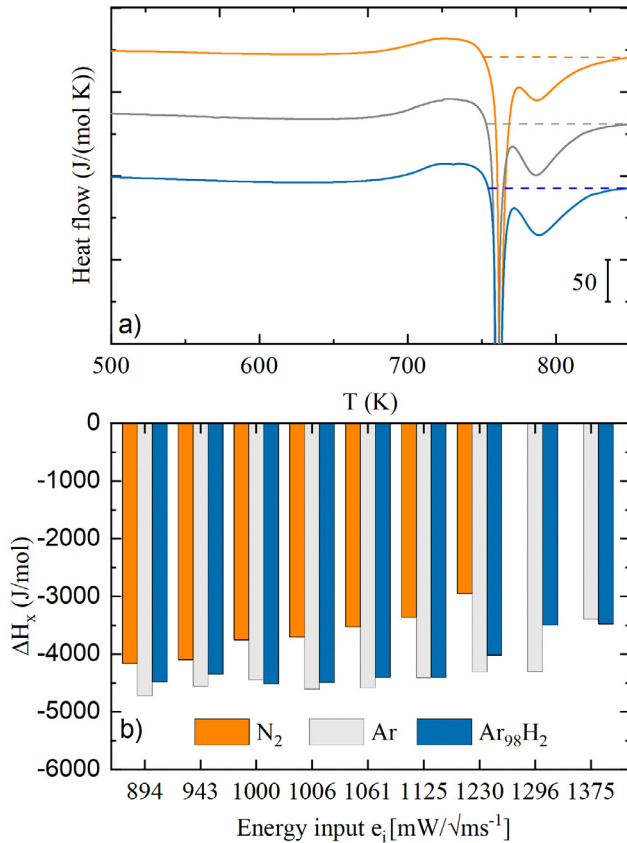


Fig. 3. (a) exemplary DSC measurements, the dotted lines indicate the integration interval (b) Enthalpy of crystallization H_x in dependence of e_i and the introduced gases N₂, Ar, and Ar₉₈H₂

Three representative XRD results are pictured in Fig. 4. For $e_i = 894 \text{ mW}/\sqrt{m \cdot s^{-1}}$, the diffractogram of the sample formed under Ar shows an amorphous halo without crystalline reflexes, indicating a glassy microstructure within the detection limits. In comparison, the usage of N₂ and Ar₉₈H₂ led to crystalline reflexes, which corresponds well to those of the Cu₂Zr₄O phase reported in the literature [11, 12]. With increasing e_i , the amount and intensity of crystalline reflexes increase for all process gases whereas N₂-formed samples feature the most distinct peaks over the entire e_i range. [11, 12]. As the energy input increases, the size and dwell time of the melt pool increases. Thus, the interaction time and reactive area between the molten material and shielding gas is enhanced, fostering reactions with the surrounding atmosphere. [29] Consequentially, also the heat-affected zone grows, and the effect of heat treatment in the subsequent layers increases the timespan for nucleation and growth of Cu-Zr-phases and oxides in the material. It is noticeable that despite the rather high reactivity of N₂, the formation of oxides is predominant compared to the formation of nitrides. Since the residual oxygen contamination within the chamber ($0.05 \pm 0.02 \text{ vol.}\%$) was held constant and the powder material was not reused over the different processes, an additional oxygen uptake resulting from the N₂ flow is concluded. Compared to that, samples built under Ar-based (Ar, Ar₉₈H₂) shielding gases exhibited minor crystalline fractions. Although the amount of impurities in the Ar₉₈H₂ gas mixture is within the same

scale as the investigated N₂, the oxide formation is significantly reduced. This might be attributed to an oxygen reduction caused by the hydrogen content. However, the effect vanishes compared to the high-purity Ar gas used in this study.

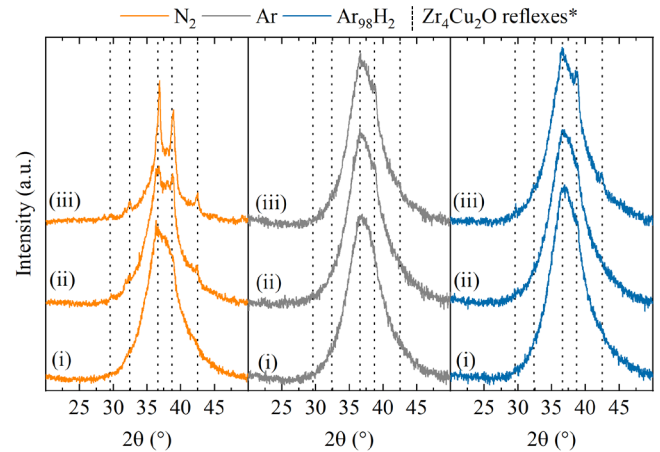


Fig. 4. X-ray diffractograms of under (a) N₂, (b) Ar, and (c) Ar₉₈H₂ processed samples with e_i of: (i) 894 (ii) 1061 (iii) 1230 $\text{mW}/\sqrt{\text{ms}^{-1}}$, with Θ as glancing angle (Bragg-angle). The dotted lines represent the reflexes of Zr₄Cu₂O (*as reported in [11, 12])

3.3. Influence on the mechanical properties

The observed increase of the crystalline fraction accompanied by the usage of N₂ processed samples was accompanied by enhanced mean hardness values as illustrated in Fig. 5. The hardness further rises with the energy input under N₂ from 451 ± 8 to $496 \pm 9 \text{ HV5}$.

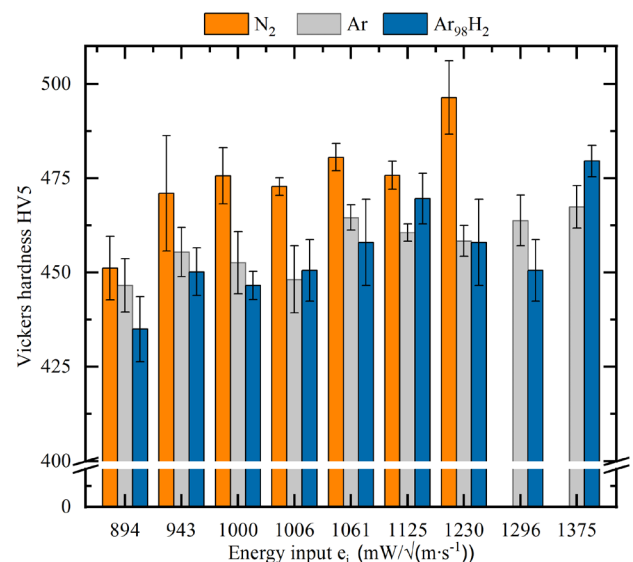


Fig. 5. (a) Mean Vickers hardness in dependence of the energy input e_i and the used shielding gases N₂, Ar, and Ar₉₈H₂.

The correlation between energy input and hardness with argon-based shielding gases is distinctive with higher e_i where a significant hardness increase is observed with $1375 \text{ mW}/\sqrt{\text{ms}^{-1}}$, corresponding to the decrease of the

crystallization enthalpy and formation of $\text{Cu}_2\text{Zr}_4\text{O}$ -oxides as seen in Fig. 3 and Fig. 4. Further fluctuating hardness values are also attributed to the varying relative densities.

The impact of the microstructural condition on the flexural strength is illustrated in Fig. 6. All investigated bending beams exhibited brittle fracture without plastic deformation and comparable young's modulus of ~ 82 GPa. Bending beams built in Ar showed a flexural strength of 1684.3 ± 115.5 MPa which is in good correspondence with the observations from Wegner et al in [14]. In comparison, beams processed under Ar_{98}H_2 exhibited a slightly increased flexural strength of 1692.7 ± 49.7 MPa. The N_2 -atmosphere led to a severe reduction of flexural bending strength of $\sim 30\%$ to 1167.3 ± 107.9 MPa. Since the relative density values of the Ar_{98}H_2 and N_2 samples are equal at the applied energy input level of $894 \text{ mW}/\sqrt{\text{m} \cdot \text{s}^{-1}}$, the significant weakening is

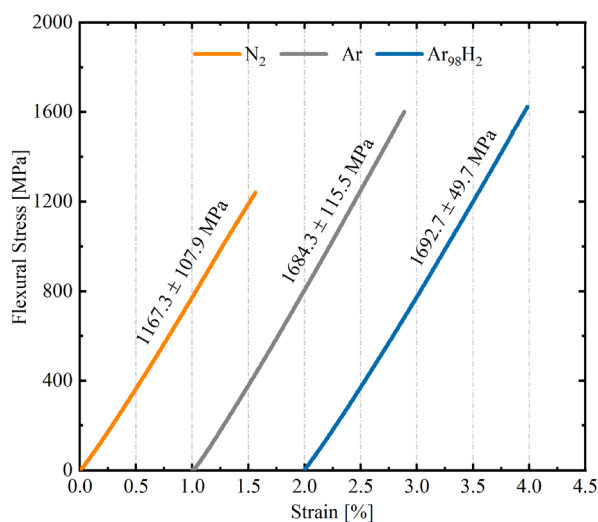


Fig. 6. Mean stress-strain curves averaged over four measurements for each applied shielding gas. The samples are processed with an e_i of $894 \text{ mW}/\sqrt{\text{m} \cdot \text{s}^{-1}}$.

attributed to the increased crystalline fraction in this context. One can conclude that the present residual porosity of $\sim 1\%$ has a minor influence on the flexural strength, compared to the microstructural weakening through the crystalline fraction [14]. It is noteworthy, that although the applied parameter set revealed first signs of crystallization within the XRD and DSC-measurements in the material processed under Ar_{98}H_2 , no distinct weakening of the material was present. However, measuring the hydrogen and oxygen uptake during the process is further necessary to quantify the impact of hydrogen addition in the process gas.

5. Conclusion

The influence of three different shielding gases (N_2 , Ar, and Ar_{98}H_2) on the PBF-LB/M-process and the resulting structural, mechanical, and thermophysical properties of $\text{Zr}_{59.3}\text{Cu}_{28.8}\text{Al}_{10.4}\text{Nb}_{1.5}$ were investigated. Applying high purity Ar as shielding gas led to fully amorphous processing with a relative density of 99.8%. The usage of N_2 -shielding gas led to a reduction of the processable parameter range

accompanied by severe cracking and crystallization. However, no reaction of nitrogen with the alloy was observed, instead the formation of $\text{Zr}_4\text{Cu}_2\text{O}$ was observed as the primary phase formation for all investigated gases. Despite a similar impurity as the applied N_2 the introduced Ar_{98}H_2 as shielding gas led to comparable results as Ar. Introducing hydrogen as a reducing element, therefore, appears as a promising approach to reduce the influence of oxygen impurities in the introduced gases. Therefore, further investigations with lower impurities within the gas mixture and higher H contents will be performed.

Acknowledgements

The authors would like to thank Dr.-Ing. Stefanie Hanke from the Chair of Materials Engineering at the University of Duisburg-Essen for their extensive support in carrying out metallography. We also want to thank Nico Neuber, Patrick Stiglmaier, and Martina Stemmler from the Chair of Metallic Materials for help in sample preparation, analysis, and fruitful discussions. Further thanks also go to Moritz Stolpe from Heraeus GmbH and Dominik Bauer from Linde AG for the provision of the powder material and gas. The research was conducted within the Industrial Community Research (IGF) project 19927 N of the Association for Research in Precision Mechanics, Optics and Medical Technology (F.O.M), Werderscher Markt 15, 10117 Berlin. The project is funded by the German Federal Ministry of Economics and Energy within the framework of the AiF's Programme for the Promotion of Industrial Community Research (on the basis of a resolution passed by the German Bundestag).

References

- [1] Wohlers Associates. Wohlers report 2019: 3D printing and additive manufacturing state of the industry. Fort Collins, Colorado: Wohlers Associates; 2019.
- [2] Yap CY, Chua CK, Dong ZL, Liu ZH, Zhang DQ, Loh LE et al. Review of selective laser melting: Materials and applications. *Applied Physics Reviews* 2015;2(4):41101
- [3] Chen S, Tong Y, Liaw P. Additive Manufacturing of High-Entropy Alloys: A Review. *Entropy* 2018;20(12):937.
- [4] Li XP, Ji G, Chen Z, Addad A, Wu Y, Wang HW et al. Selective laser melting of nano-TiB 2 decorated AlSi10Mg alloy with high fracture strength and ductility. *Acta Materialia* 2017;129:183–93.
- [5] Li XP, Roberts MP, O'Keeffe S, Sercombe TB. Selective laser melting of Zr-based bulk metallic glasses: Processing, microstructure and mechanical properties. *Materials & Design* 2016;112:217–26.
- [6] Pauly S, Schricker C, Scudino S, Deng L, Kühn U. Processing a glass-forming Zr-based alloy by selective laser melting. *Materials & Design* 2017;135:133–41.
- [7] Yang C, Zhang C, Xing W, Liu L. 3D printing of Zr-based bulk metallic glasses with complex geometries and enhanced catalytic properties. *Intermetallics* 2018;94:22–8.
- [8] Inoue A, Shen B, Koshiba H, Kato H, Yavari AR. Cobalt-based bulk glassy alloy with ultra high strength and soft magnetic properties. *Nature Materials* 2003;2(10):661–3.
- [9] Kok Y, Tan XP, Wang P, Nai MLS, Loh NH, Liu E et al. Anisotropy and heterogeneity of microstructure and mechanical properties in metal additive manufacturing: A critical review. *Materials & Design* 2018;139:565–86.
- [10] Jung HY, Choi SJ, Prashanth KG, Stoica M, Scudino S, Yi S et al. Fabrication of Fe-based bulk metallic glass by selective laser melting: A parameter study. *Materials & Design* 2015;86:703–8.
- [11] Marattukalam JJ, Pacheco V, Karlsson D, Riekehr L, Lindwall J, Forsberg F et al. Development of process parameters for selective laser

- melting of a Zr-based bulk metallic glass. *Additive Manufacturing* 2020;33:101124.
- [12] Pacheco V, Karlsson D, Marattukalam JJ, Stolpe M, Hjärvarsson B, Jansson U et al. Thermal stability and crystallization of a Zr-based metallic glass produced by suction casting and selective laser melting. *Journal of Alloys and Compounds* 2020;825:153995.
- [13] Bordeenithikasem P, Stolpe M, Elsen A, Hofmann DC. Glass forming ability, flexural strength, and wear properties of additively manufactured Zr-based bulk metallic glasses produced through laser powder bed fusion. *Additive Manufacturing* 2018;21:312–7.
- [14] Wegner J, Frey M, Stiglmair P, Kleszczynski S, Witt G, Busch R. MECHANICAL PROPERTIES OF HONEYCOMB STRUCTURED ZR-BASED BULK METALLIC GLASS SPECIMENS FABRICATED BY LASER POWDER BED FUSION. *SAJIE* 2019;30(3).
- [15] Wang XJ, Zhang LC, Fang MH, Sercombe TB. The effect of atmosphere on the structure and properties of a selective laser melted Al–12Si alloy. *Materials Science and Engineering: A* 2014;597:370–5.
- [16] Dai D, Gu D. Effect of metal vaporization behavior on keyhole-mode surface morphology of selective laser melted composites using different protective atmospheres. *Applied Surface Science* 2015;355:310–9.
- [17] King WE, Anderson AT, Ferencz RM, Hodge NE, Kamath C, Khairallah SA et al. Laser powder bed fusion additive manufacturing of metals; physics, computational, and materials challenges. *Applied Physics Reviews* 2015;2(4):41304.
- [18] Pazuon C, Hryha E, Forêt P, Nyborg L. Effect of argon and nitrogen atmospheres on the properties of stainless steel 316 L parts produced by laser-powder bed fusion. *Materials & Design* 2019;179:107873.
- [19] Liu Z, Li R, Wang H, Zhang T. Nitrogen-doping effect on glass formation and primary phase selection in Cu–Zr–Al alloys. *Journal of Alloys and Compounds* 2011;509(16):5033–7.
- [20] Brezovnik A. J. Tušek, M. Suban: Influence of hydrogen in argon as a shielding gas in arc welding of high-alloy stainless steel.
- [21] Dong F, Su Y, Luo L, Wang L, Wang S, Guo J et al. Enhanced plasticity in Zr-based bulk metallic glasses by hydrogen. *International Journal of Hydrogen Energy* 2012;37(19):14697–701.
- [22] King WE, Barth HD, Castillo VM, Gallegos GF, Gibbs JW, Hahn DE et al. Observation of keyhole-mode laser melting in laser powder-bed fusion additive manufacturing. *Journal of Materials Processing Technology* 2014;214(12):2915–25.
- [23] Scipioni Bertoli U, Wolfer AJ, Matthews MJ, Delplanque J-PR, Schoenung JM. On the limitations of Volumetric Energy Density as a design parameter for Selective Laser Melting. *Materials & Design* 2017;113:331–40.
- [24] T.W. Eagar N-ST. Temperature fields produced by traveling distributed heat sources. *Welding Journal* 1983(62):346–55.
- [25] Pooriya Dastranjy Nezhadfar, Mohammad Masoomi, Scott Thompson, Nam Pham, and Nima Shamsaei. Mechanical Properties of 17-4 Ph Stainless Steel Additively Manufactured Under Ar and N₂ Shielding Gas.
- [26] Masmoudi A, Bolot R, Coddet C. Investigation of the laser–powder–atmosphere interaction zone during the selective laser melting process. *Journal of Materials Processing Technology* 2015;225:122–32.
- [27] Masoomi M, Pegues JW, Thompson SM, Shamsaei N. A numerical and experimental investigation of convective heat transfer during laser-powder bed fusion. *Additive Manufacturing* 2018;22:729–45.
- [28] Heinrich J, Busch R, Nonnenmacher B. Processing of a bulk metallic glass forming alloy based on industrial grade Zr. *Intermetallics* 2012;25:1–4.
- [29] Na T-W, Kim WR, Yang S-M, Kwon O, Park JM, Kim G-H et al. Effect of laser power on oxygen and nitrogen concentration of commercially pure titanium manufactured by selective laser melting. *Materials Characterization* 2018;143:110–7.